

Generative adversarial neural networks for simulating neutrino interactions

José L. Bonilla,^{*} Krzysztof M. Graczyk,[†]

Artur M. Ankowski, Rwik Dharmapal Banerjee, Beata E. Kowal, Hemant Prasad, and Jan T. Sobczyk

Institute for Theoretical Physics, University of Wrocław, plac Maxa Borna 9, 50-204, Wrocław, Poland

(Dated: February 28, 2025)

We propose a new approach to simulate neutrino scattering events as an alternative to the standard Monte Carlo generator approach. Generative adversarial neural network (GAN) models are developed to simulate neutrino-carbon collisions in the few-GeV energy range. The models produce scattering events for a given neutrino energy. GAN models are trained on simulation data from NuWro Monte Carlo event generator. Two GAN models have been obtained: one simulating only quasielastic neutrino-nucleus scatterings and another simulating all interactions at given neutrino energy. The performance of both models has been assessed using two statistical metrics. It is shown that both GAN models successfully reproduce the event distributions.

I. INTRODUCTION

Monte Carlo (MC) event generators are indispensable tools in neutrino oscillation experimental analysis. Ongoing and future experimental collaborations, such as T2K [1], MicroBooNE [2], DUNE [3], and Hyper-Kamiokande [4], use accelerator-based neutrino sources with broad neutrino energy spectra. Their goal is to perform precise measurements of the Standard Model (SM) oscillation parameters in the hope of gaining sensitivity to effects beyond the SM. However, the probability of neutrino oscillations is a rapidly changing function of neutrino energy, and its value cannot be directly accessed.

Thus, oscillation analyses require procedures to reconstruct neutrino energy from the detected final-state particles. These procedures rely heavily on Monte Carlo (MC) simulations [5], which must incorporate models for all relevant physical processes, including various types of interactions on bound nucleons (or, at higher energies, on quarks), contributions from two-body currents, and coherent neutrino-nucleus reactions. Additionally, final state interactions (FSI), i.e. secondary interactions of hadrons inside nuclei, must be accounted for.

Over the past ~ 20 years, significant efforts have been made to develop neutrino MC generators for modeling neutrino interactions with matter. Existing MC generators include those used directly by experimental groups, such as NEUT [6] and GENIE [7], as well as models developed by theoretical groups, such as GiBUU [8], NuWro [9], and Achilles [10].

MC generators for events (in particle and nuclear physics) serve as a bridge between theory and experiment [11]. Monte Carlo simulations are employed at every stage of an experimental study, including the production of the neutrino flux, interactions within a detector,

and the detector's response. In this paper, we focus entirely on neutrino interactions inside the detector.

The MC generators, equipped with implementations of theoretical and phenomenological models, are often tuned to match experimental data. Theoretical models implemented in generators typically rely on uncertain internal parameters adjusted using available experimental data. However, these procedures cannot fully account for limitations stemming from theoretical models, which involve many approximations, particularly in the case of nuclear effects. Therefore, it would be beneficial to develop alternatives to existing MC event generators that can learn directly from available experimental cross-section data and modify their predictions accordingly. As a result, efforts have been made to explore new approaches for developing alternatives to standard MC generators. A novel approach has recently emerged: leveraging advanced artificial intelligence (AI) models to dynamically adapt to experimental data, enabling highly effective simulations of physical phenomena. Machine-learning methods have been applied to study and model neutrino-nucleus scattering and related electron-nucleus processes. These applications include extracting information about the axial content of the nucleon [12], modeling electron-nucleus scattering cross-sections [13–16], and accelerating sampling from given differential cross-section distributions [17].

This paper explores, adapts, and advances modern machine-learning techniques for simulating neutrino-nucleus scattering events. We focus on generative adversarial networks (GANs) [18]. The GAN technique enables training a neural network that learns to generate data produced by an unknown or poorly understood mechanism. A successful generative model takes an input latent vector drawn from a given distribution in the latent space (typically a Gaussian distribution) and generates samples that match the characteristics of the training data.

Generative deep learning models have demonstrated their effectiveness across various domains, including image generation [19], image super-resolution, and semi-supervised learning [20, 21]. A comprehensive review of GANs can be found in Ref. [22]. The GAN technique

^{*} joseluis.bonillaramirez@uwr.edu.pl

[†] krzysztof.graczyk@uwr.edu.pl

is also promising for MC generators of particle interactions [23]. Indeed, the GANs have been adapted to simulate parton showers [24, 25] in high energy collisions, as well as to model hadronization [26–28]. An effort has also been made to adapt GANs to simulate collisions of highly energetic electrons with proton [29].

This paper applies the GAN technique to simulate charged current (CC) neutrino-carbon scattering. We consider two cases. First, we test the applicability of our approach to quasielastic (QE) scattering. Then, we extend our study to include all interaction modes at a given neutrino energy. In both cases, the GAN takes neutrino energy as input and generates the charged lepton kinematics. The model is applicable to neutrino energies ranging from a few hundred MeV to tens of GeV, which are typical for neutrino oscillation experiments.

For our study, we utilize the NuWRO MC generator, which has been under development since 2004 [9, 30, 31]. It is optimized for the energy range characteristic of neutrino oscillation experiments using accelerator-based neutrino sources, spanning from hundreds of MeV to tens of GeV. The GAN is trained on NuWro-generated data to produce scattering events. Developing a successful GAN model is more challenging than standard supervised learning [32]. Therefore, we assess the model’s performance using two metrics to evaluate its effectiveness: the mean absolute value of pulls and the Earth Mover’s Distance (EMD) [33].

The paper is organized as follows: Sec. II introduces the GAN techniques and describes the technical details of our approach; Sec. III presents numerical results; Sec. IV summarizes the paper.

II. METHOD

We aim to obtain the deep neural network (DNN) that generates neutrino-nucleus scattering events. As an illustrative example, we consider muon neutrino charged current interactions with a carbon target. The DNN model is trained (optimized) to learn the underlying probability distribution. As a source of information on neutrino-carbon scattering, we employ the NuWRO MC generator.

In realistic simulations, one provides the input information and models the neutrino-nucleus collisions in all relevant channels. As an output, one obtains a distribution of events, including complete information about the final particles. The number of final particles can vary from event to event. Obtaining a generative network that does the same work as “classical” MC generators is a difficult task. Therefore, in this first effort, we consider a GAN that generates only the final lepton’s kinematics, and the flux spectrum is uniform.

The procedure for getting the model is the following:

- define the lepton variables generated by the model;
- obtain the training data set;

- construct GANs for analysis;
- perform optimization;
- test model against data not used in the optimization stage.

Each step is described in the following subsections.

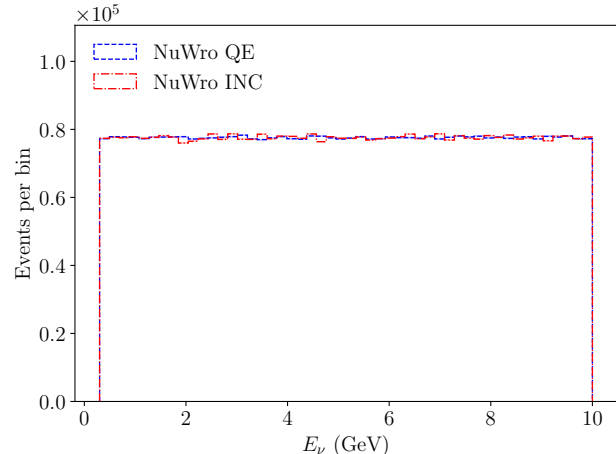


FIG. 1. Energy distribution of the QE (blue dashed line) and INC (red dashed-dotted line) training samples from NuWRO.

II.1. Data and kinematic settings

We consider CC QE and inclusive (INC) scattering of muon neutrinos off carbon. The QE and INC data are obtained from a simulation done with the NuWRO MC event generator, using the spectral function approach to model the nucleus in the QE channel [34] and the local Fermi gas in other channels. In the QE case, the generated events contain muons and nucleons or sometimes pions due to the final state interaction effects. In the INC case, the final states contain muons and a variety of mesons and baryons. In both types of events, this study only considers the muon’s kinematics.

Let us denote the neutrino energy by E_ν . The outgoing muon is characterized by its energy E_μ and momentum \mathbf{p}_μ . The angle between the neutrino and muon momenta is denoted by θ .

The complete description of muon kinematics requires three independent variables, such as the components of the muon momentum. However, due to the rotational symmetry of the system relative to the axis defined by the neutrino beam, two independent variables are sufficient to generate the muon kinematics for unpolarized targets. These could be chosen: the muon energy E_μ and the longitudinal momentum $p_{\mu,z}$ (along the neutrino momentum) or E_μ and the angle θ .

The variables $p_{\mu,z}$, E_μ , and θ are related as follows:

$$p_{\mu,z} = \sqrt{E_\mu^2 - m_\mu^2} \cos \theta, \quad (1)$$

where m_μ is the muon mass.

Our goal is to construct a model that, for a given energy E_ν , generates a required distribution of the events. We consider neutrino energies from $E_{\nu,min} = 300$ MeV to $E_{\nu,max} = 10$ GeV.

The neural networks work most efficiently when input variables are in the range $\sim (-1, 1)$. Hence, we introduce the re-scaled energy variable:

$$E'_\nu = 2 \frac{E_\nu - E_{\nu,min}}{E_{\nu,max} - E_{\nu,min}} - 1, \quad (2)$$

then $E'_\nu \in [-1, 1]$.

We optimize the GAN model on events with uniform energy distribution to obtain a model that accurately predicts neutrino events for any energy in the considered range. We generate a large training set such that $\sim 40k$ events correspond to any energy interval of 100 MeV, with a total of 3.88M events comprising each training sample. The energy distributions of the events used to train both the QE and INC models are shown in Fig. 1.

As explained above, the network generates two variables that define the muon kinematics. After considering various options, we use a pair (E'_μ, θ') , given by:

$$E'_\mu = 2\sqrt{1 - \frac{E_\mu - m_\mu}{\Delta E}} - 1, \quad \Delta E = E_\nu^- - m_\mu \quad (3)$$

$$\theta' = 2\sqrt{\frac{\theta}{\pi}} - 1, \quad (4)$$

where $E_\nu^- = E_\nu - 9.8$ MeV is used to ensure a tighter upper bound. Both variables take values ranging approximately from -1 to 1 .

II.2. GAN for event generation

The objective of the GAN approach is to develop a model (usually DNN) such that, given a random latent vector, it predicts outputs that belong to the “true”¹ distribution of samples. In this context, we are using a conditional GAN (CGAN) [35], which incorporates neutrino energy and the random latent vector.

To obtain a successful generator G, one introduces a discriminator D, another DNN trained to discriminate between samples obtained from the generator and the “true” samples from the training dataset. Both generator and discriminator models are optimized. The discriminator learns to distinguish between “true” and GAN events, while the generator improves in “mimicking true” events discriminator.

We implement models and perform numerical analysis using the Keras 2.15 package [36]. Note that the architectures of both QE and INC models are similar. Let

¹ In the case of present studies “true” denotes NuWRO generated event.

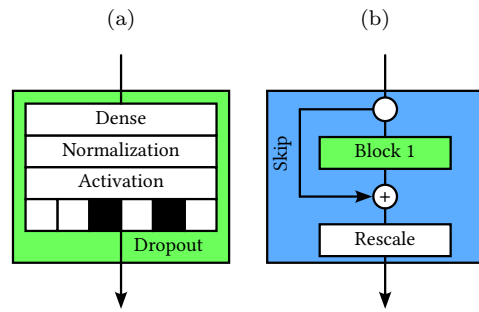


FIG. 2. Building blocks of the generators and discriminators, **Block 1** (a) and **Block 2** (b). The second block is obtained from **Block 1** by adding a skip connection and rescaling layer.

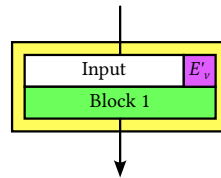


FIG. 3. The condition E'_ν is concatenated to the inputs of a block of the INC network. The **Block 1** (see Fig. 2) with above modification is called **Block 3**. If we add a skip connection and rescale layer to a **Block 3**, one obtains **Block 4**.

us denote the discriminator and generative models for QE(INC) data by D-QE(INC) and G-QE(INC), respectively.

The common elements of the basic building block are shown in Fig. 2. The basic module, **Block 1**, of our DNNs consists of a fully connected (dense) layer, followed by a normalization [37], an activation layer, and a dropout layer (with a rate of 10%); see Fig. 2(a). If the input and output of the **Block 1** in the main body of the network have the same dimension, a skip connection [38] from the input to the output is added (see Fig. 2(b)) to form **Block 2**. The output of this block is rescaled by factors we discuss below.

We also employ a variation of **Block 1** (2), called **Block 3** (4), in which the information about the condition E'_ν is concatenated to its input right before the dense layer, as shown in Fig. 3. **Block 1**(2) with extra E'_ν input will be called **Block 3**(4), respectively. Note that these blocks are used only by INC models.

The input latent vector \mathbf{x} is drawn from the standard normal distribution $N(0, 1)$. Generators G-QE and G-INC transform the input latent vector and neutrino energy similarly. Namely, both \mathbf{x} and E'_ν are transformed independently by a fully connected dense layer (with a linear activation function) to ensure that the neutrino energy is as important as the latent vector; see Fig. 4(a). Then, both layers are concatenated together, processed by **Block 1**, and sent to the *main body* of the network. The main body of G-QE(INC) consists of one

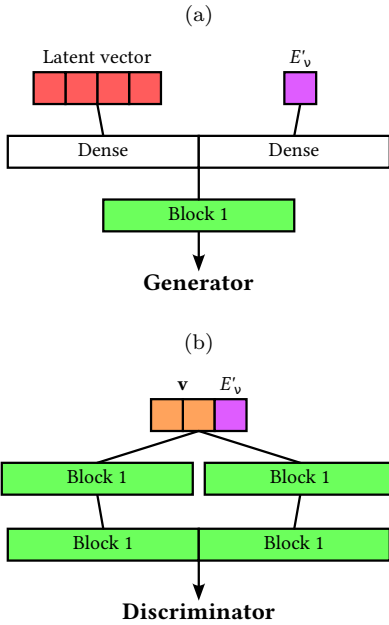


FIG. 4. The input block of the generators (a) and discriminators (b). The generator independently transforms the latent vector and E'_ν by a linear dense layer. Then, both outputs are concatenated and sent to a **Block 1**. The discriminator directly concatenates \mathbf{v} and E'_ν , then processes them in two parallel branches with two consecutive blocks.

Block 1(3) followed by one **Block 2**(4). Consequently, there are a total of three blocks chained in G-QE(INC). The last section consists of the dense layer with a two-dimensional output activated with **tanh** function.

The input of D-QE(INC) is either the NUWRO sample vector (\mathbf{v}, E'_ν) or the output of the generator $(G(\mathbf{x}, E'_\nu), E'_\nu)$. The input is transformed in parallel by two branches of the same architecture (see Fig. 4(b)). Each branch consists of a sequence of two **Blocks 1**. Then, the outputs of both branches are concatenated and transformed by the *main body*, which is made by one **Block 1**(3) and a sequence of three **Blocks 2**(4). The neural network has a total depth of six **Blocks**. The last section of the discriminator is a fully connected layer with a single neuron and **linear** activation function (a **sigmoid** is applied on the output when it contributes to the loss).

We apply **leaky ReLU** [39] activation functions for the D-QE and G-QE models. Since the INC samples are more complex than the QE ones, we improved the network architectures to converge with the optimization process. We observed that the discriminator has to be more robust than the generator to feed relevant information to the generator. With this in mind, the activation functions in the blocks were changed to **ReLU** [40] for G-INC and **PReLU** [41] for D-INC. As remarked, **Blocks 1 and 2** of the central bodies of the INC networks are replaced by **Blocks 3 and 4**. The rescaling of **Blocks 4** is 1/2 in the INC model, and there is no

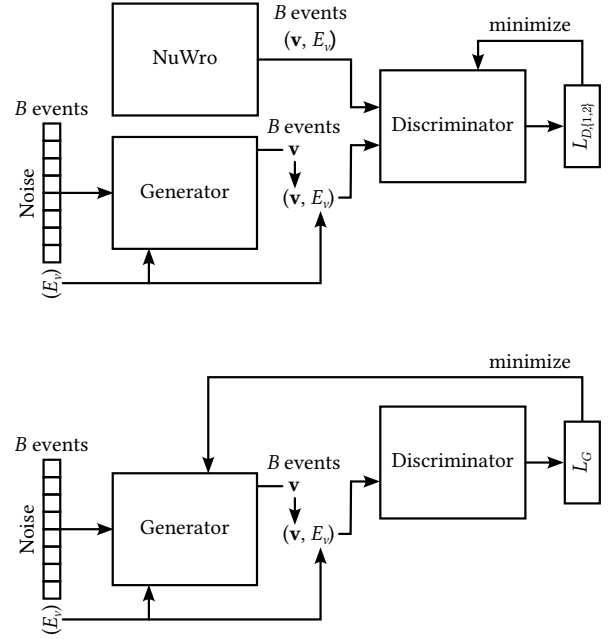


FIG. 5. The top graph shows the iteration step in which the discriminator trained to recognize the NUWRO and the network-generated samples. Discriminator takes for input $\mathbf{v} = (E'_\nu, \theta')$, and the condition E'_ν . The bottom graph shows the iteration step in which the generator is optimized.

rescaling in **Blocks 2** for the QE model.

Additionally, to improve the training convergence, we supplement the structure of the network architectures by including Gaussian noise layers [42], defined by standard deviation 10^{-4} for G-QE and 10^{-3} for D-QE and D-INC. The G-INC is not affected by Gaussian noise. The inputs of G-QE, D-QE, and D-INC are injected with noise, as well as each block of G-QE and D-QE after each normalization layer, while the D-INC includes it after each layer with learnable parameters (dense, normalization layer, and **PReLU**). The last dense layer of G-QE is not affected, but the output of the last dense layer of both D-QE and D-INC are also altered by noise. It is worth noting that **Blocks 3 and 4** of D-INC are fed with the noisy E'_ν .

The blocks of the G-QE and the D-QE have 100 neurons, except for the first **Block 1** of G-QE, which has 200 neurons, and the two dense layers of each initial pair of branches of the D-QE, which consists of 50 neurons. Similarly, the G-INC comprises blocks and dense layers of 100 neurons, but the first block has 200 neurons (just as the G-QE). The D-INC model has more neurons in the blocks than its QE counterpart. In D-INC, most blocks consist of 141 neurons, but the first two dense layers in the initial branches have 70 neurons each.

II.3. Optimization scheme

To train the model, we use the cross-entropy loss function given by three contributions

$$L_{D,1}(G) = -\frac{1}{B} \sum_{i=1}^B \log[D(G(\mathbf{x}_i, E_{\nu,i}), E_{\nu,i})] \quad (5)$$

$$L_{D,2}(\mathbf{v}) = -\frac{1}{B} \sum_{j=1}^B \log[1 - D(\mathbf{v}_j, E_{\nu,j})] \quad (6)$$

$$L_G(G) = -\frac{1}{B} \sum_{k=1}^B \log[1 - D(G(\mathbf{x}_k), E_{\nu,k})], \quad (7)$$

where B is the number of samples in the mini-batch.

GANs are optimized using the so-called mini-max framework [43]. Hence, a successful model is a result of a balance between two losses: of the discriminator (5) and (6) and of the generator (7). The Eq. (5) is computed on “fake” data generated by G , whereas the loss (6) is calculated on “true” samples obtained from NUWRO. The last loss (7) is evaluated on generated by model “fake” samples.

Both the generator and discriminator are optimized simultaneously in the minibatch configuration. In the single iteration step, the discriminator is optimized with minibatch for the NUWRO data consisting of $B = 10,000$ and $B = 1,000$ samples for the QE and INC analyses, respectively. In the same iteration step, the generator is optimized with a minibatch size of $2B$. The iterations are repeated until no data is left in the NUWRO training dataset, and a single epoch is accomplished. The training loop is shown in Fig. 5. We utilize the AdamW optimization algorithm for this purpose, a learning rate of 10^{-4} for D-QE(INC) and 10^{-5} for G-QE(INC), and $\beta_1 = 0.5$ and $\beta_2 = 0.9$.

II.4. Testing model’s quality

We monitor the optimization of the generator and discriminator by evaluating their respective loss values. In Fig. 6, we present the variation of the losses during the training of the GANs on the QE and INC data. In both cases, the loss curves converge to the same value, corresponding to the model configuration where a balance is achieved between the generator’s and the discriminator’s performance.

Another way of checking the quality of the model is by estimating the so-called *pull* [29, 44]. This technique compares the histograms of events generated by the NUWRO and the GAN.

The i -th component of the pull is given by

$$\text{pull}_i = \frac{n_{\text{NUWRO},i} - n_{\text{gan},i}}{\sqrt{\sigma_{\text{NUWRO},i}^2 + \sigma_{\text{gan},i}^2}}, \quad (8)$$

where $n_{\text{NUWRO},i}$ and $n_{\text{gan},i}$ are the bin contents at the i -th bin, and $\sigma_{\text{NUWRO},i}^2 = n_{\text{NUWRO},i}$ and $\sigma_{\text{gan},i}^2 = n_{\text{gan},i}$ are statistical uncertainties. The bin contents of a histogram are expected to follow the Poisson distribution. As the G event distribution gets closer to NUWRO’s, then Eq. (8) defines random variable that follows a standard normal distribution $N(0, 1)$ for large $n_{\text{NUWRO},i}$ and $n_{\text{gan},i}$. For a random variable $x \sim N(0, 1)$, the expected value of $|x|$ is

$$\mathbb{E}_{x \sim N(0,1)}[|x|] = \sqrt{2/\pi} \approx 0.80. \quad (9)$$

To check the goodness of the model, we evaluate the mean of the absolute value of pulls

$$\text{MAP} = \frac{1}{K} \sum_{i=1}^K |\text{pull}_i|, \quad (10)$$

where K is the number of bins that satisfy $n_{\text{nuw},i} \neq 0$ and $n_{\text{gan},i} \neq 0$. We checked that the MAP between two (normalized) NUWRO samples is ~ 0.8 .

The MAP metric is computed using histograms of the joint E'_μ and θ' distribution, as shown in Figs. 7 and 8. To reduce the bias coming from extremely low statistics bins at distribution “tails”, we compute the MAP for bins for which $n_{\text{nuw},i} > 5$ and $n_{\text{gan},i} > 5$.

The Wasserstein distance, or EMD [33], is another metric to monitor the quality of the models. It measures how different two given histograms are and how much “work” one must do to redistribute one histogram into another. We evaluate this metric to monitor the quality of the training and final models. The EMD computed for two NUWRO samples is $\sim 0.03 - 0.04$.

A priori, the MAP (10) and the EMD depend on the histogram binning. To minimize its impact, \sim one million events are generated with both NUWRO and the GAN, with a binning of 50×50 in E'_ν and θ'_μ .

In Fig. 9, we show how the EMD and MAP metrics change during the training of the QE and INC models. As can be noticed, after 100 epochs, the optimization leads to the model for which the metrics begin to saturate. We stop the optimization using the MAP and EMD metrics. The best model minimizes both.

III. RESULTS

We first present the numerical results for charged-current quasielastic scattering of muon neutrinos.

The quality of the QE-GAN model and its dependence on neutrino energy is presented in Table I. We provide the values of the EMD and MAP metrics computed for several values of neutrino energies, between 0.5 and 9 GeV, as well as for a dataset with energies distributed uniformly in the energy region that covers the same energy domain as the training dataset. The performance of the G-QE model is excellent in all the considered cases.

In Fig. 7, we show the two-dimensional histograms and pull distribution of events generated by the NUWRO and

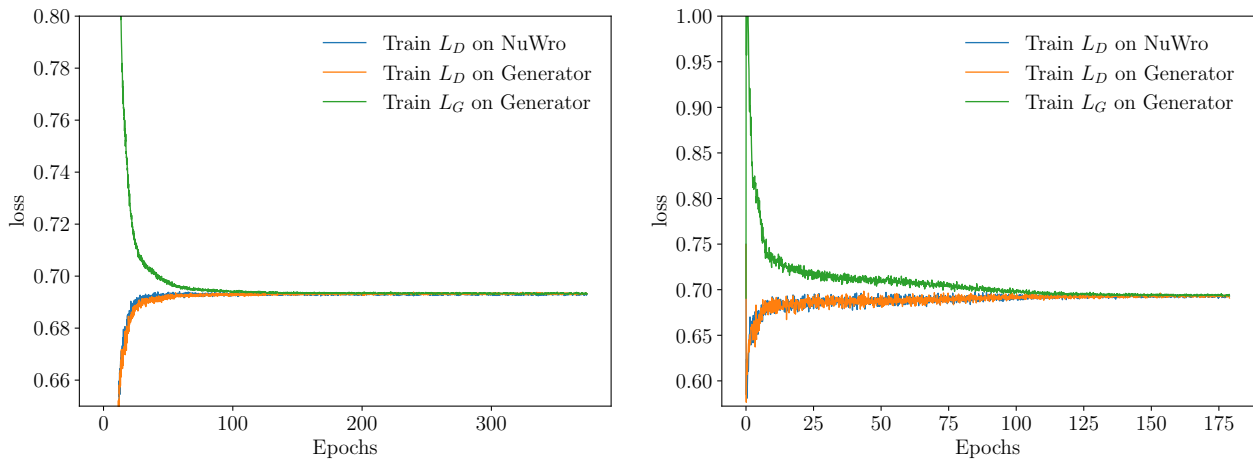


FIG. 6. The losses (5), (6), and (7) evaluated to monitor the training of the QE (left figure) and INC (right figure) GAN models.

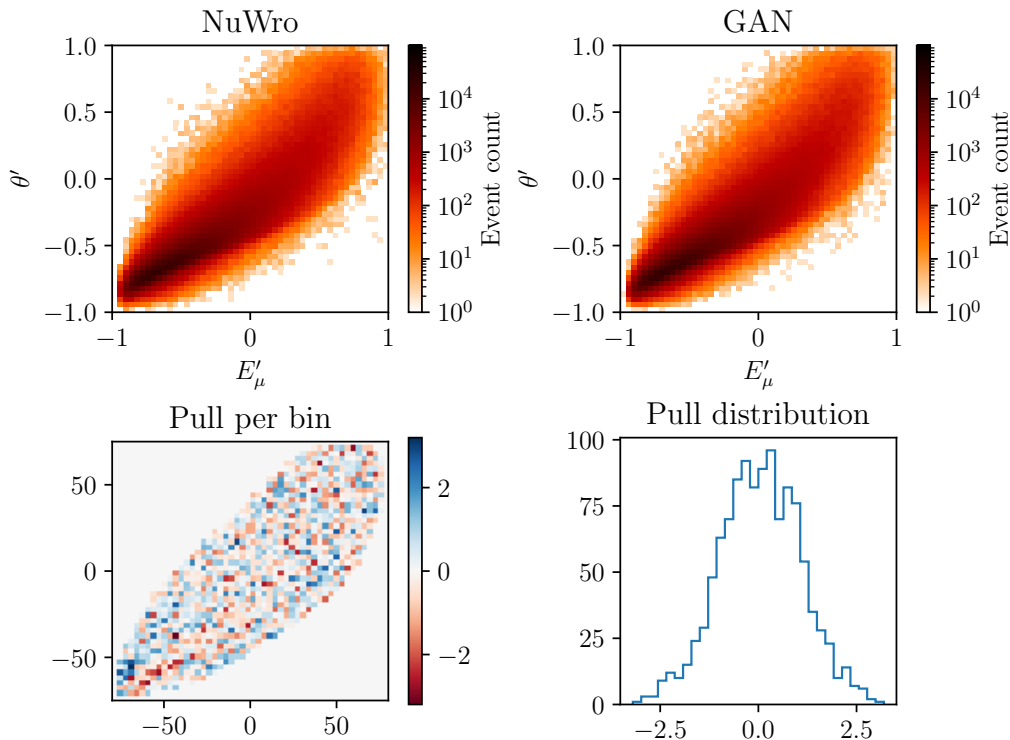


FIG. 7. Top row: NuWro (left) and GAN (right) generated samples for the QE scattering. Bottom row: Pull w/o tails per bin from NuWro and G-QE samples (left) and pull distribution (right).

G-QE that are uniformly distributed in energies from 300 MeV to 10 GeV. The pulls per bin resemble pure noise, and their distribution approaches the Gaussian shape.

The G-QE model generates event histograms that closely match those produced by the NuWro. This is demonstrated in Fig. 10, where we present event histograms for neutrino energies of 0.5, 1, and 3 GeV. The histograms are shown in terms of E'_μ and muon energy,

along with an estimate of the *pulls*. Notably, the distribution of the QE events in muon energy exhibits a single peak.

Additionally, Fig. 11 presents the dependence on θ' and θ for neutrino energies of 0.5, 1, and 5 GeV. Furthermore, we derive the longitudinal momentum as a composite variable (1) and show its event distribution in Fig. 12. The agreement between the GAN and the NuWro generated results is excellent. Note that for the comparison,

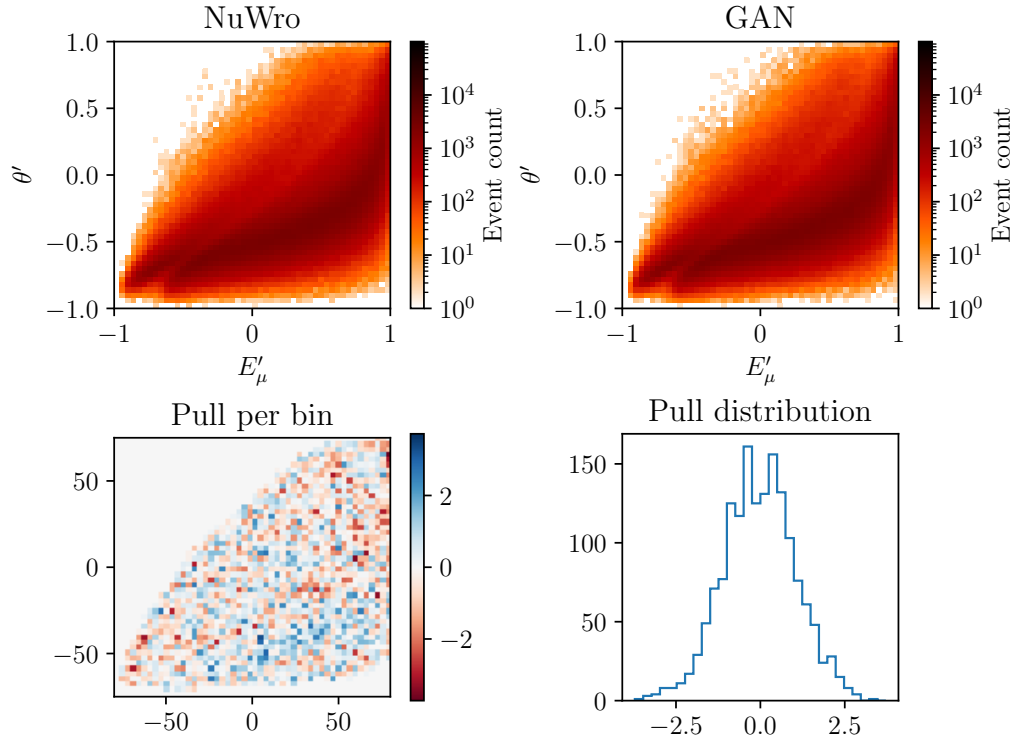


FIG. 8. Caption the same as in Fig. 7 but for inclusive scattering.

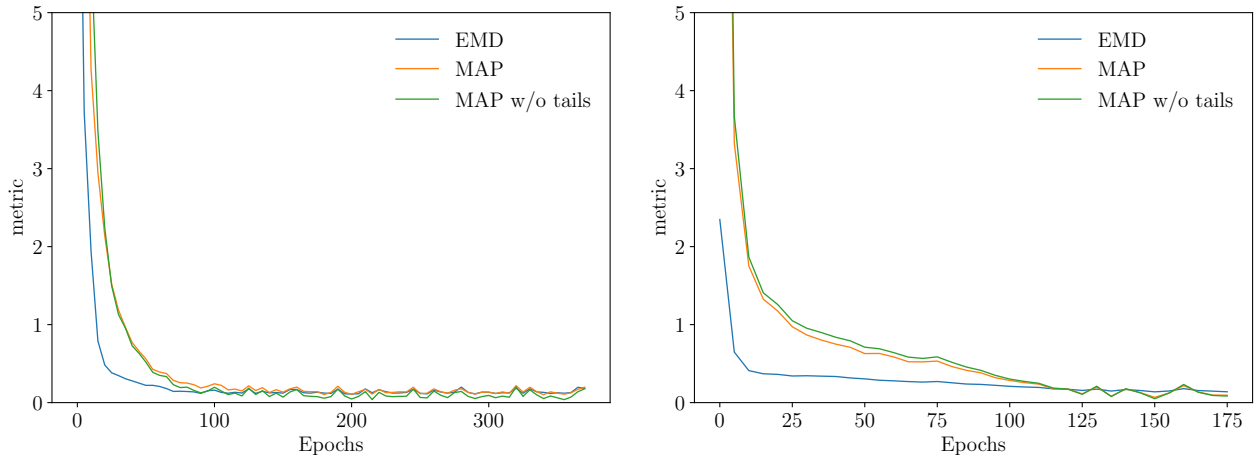


FIG. 9. The EMD and MAP metrics evaluated during training of QE (left figure) and INC (right figure) models. We plot $\text{MAP} - \sqrt{2/\pi}$. Metrics are computed every 5 epochs.

we generated a new set of the NUWRO events that were not used during training for all these tests.

Let us now discuss the INC model. As for the QE analysis, in Fig. 8, we show the two-dimensional histograms and pull distribution of INC events generated by the NUWRO and G-INC that are uniformly distributed in energies from 300 MeV to 10 GeV. Again, a good agreement is achieved between the NUWRO and G-INC generator. In Fig. 13, we plot the histograms of events generated by the G-INC and the NUWRO MC generator for neutrino

energies 1, 3 and 5 GeV for both E'_μ and E_μ .

To test if our GAN model can reproduce the QE and $\Delta(1232)$ resonance peaks equally well, let us now consider event distributions for hadronic invariant mass W defined by

$$W = \sqrt{M_N^2 + 2\omega M_N - Q^2}, \quad (11)$$

where $\omega = E_\nu - E_\mu$ is the energy transferred to the nucleus, M_N the average mass of the nucleon, and Q^2 the

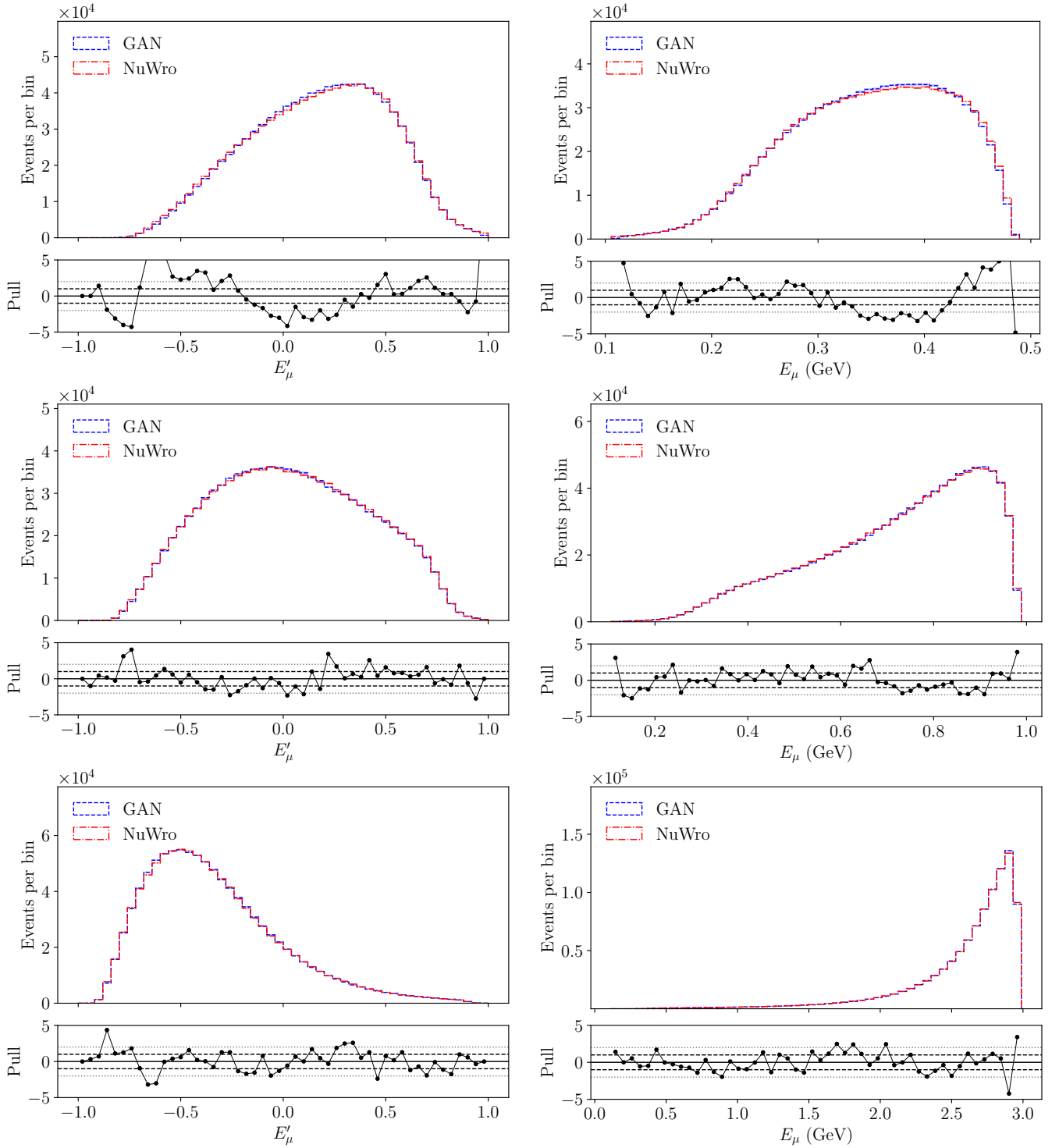


FIG. 10. Event histograms, depending on E'_μ (left column) and E_μ (right column) generated by the G-QE and NuWro for neutrino energies $E_\nu = 0.5, 1, \text{ and } 3$ GeV, from top to bottom rows, respectively.

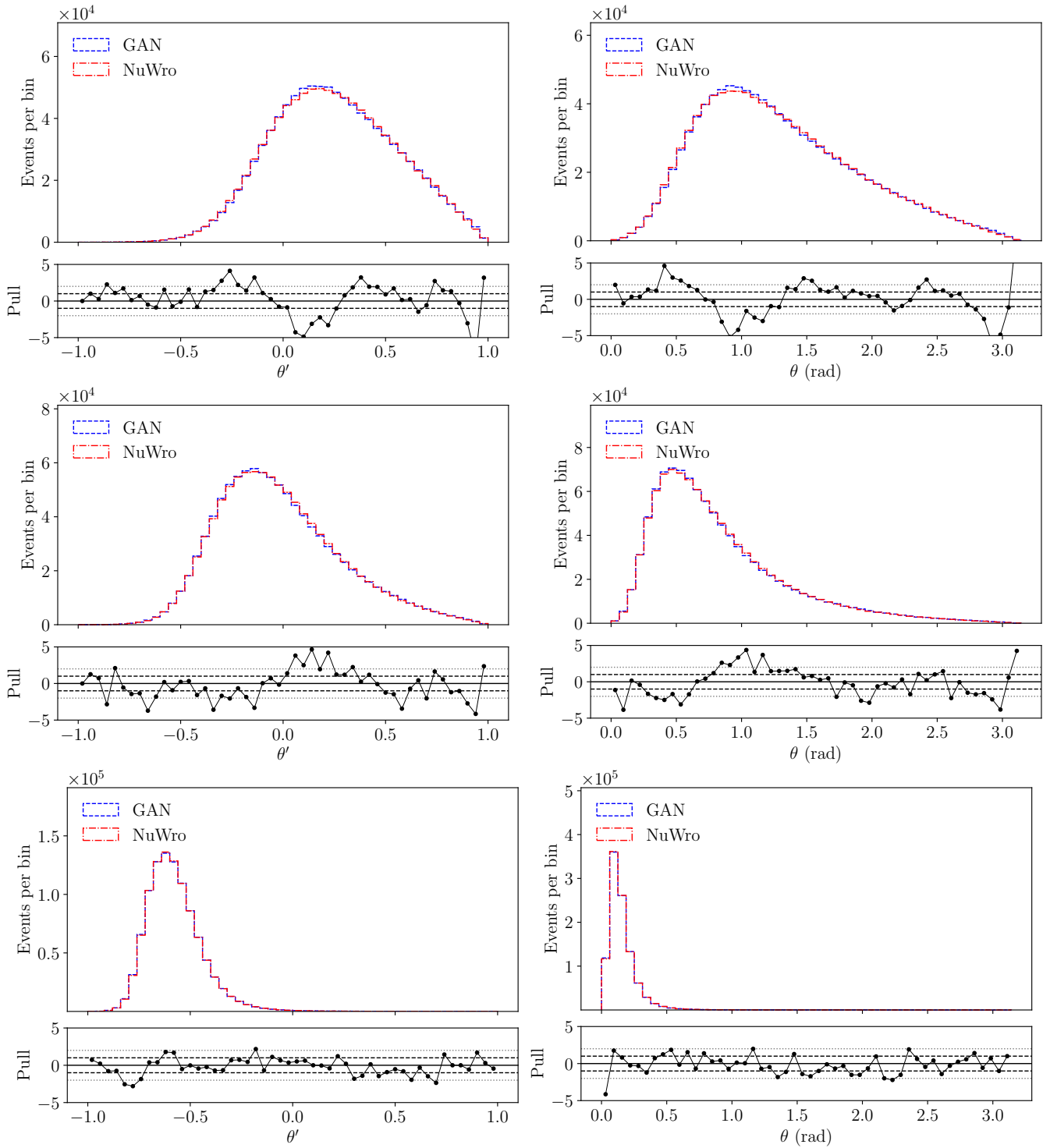


FIG. 11. Event histograms, depending on θ' (left column) and θ (right column) generated by the G-QE and NuWro for neutrino energies = 0.5, 1, and 5 GeV, shown in top, middle, and bottom rows, respectively.

four-momentum transfer

$$Q^2 = 2E_\nu(E_\mu - p_{\mu,z}) - m_\mu^2. \quad (12)$$

If one disregards the Fermi motion of nucleons in the target nucleus and their binding energies effect, the value

of W can be obtained from the muon kinematics alone.

In Fig. 14, we present the distributions of events as a function of longitudinal muon momentum $p_{\mu,z}$ and hadronic invariant mass W . We observe good agreement between the results from NuWro and G-INC for these

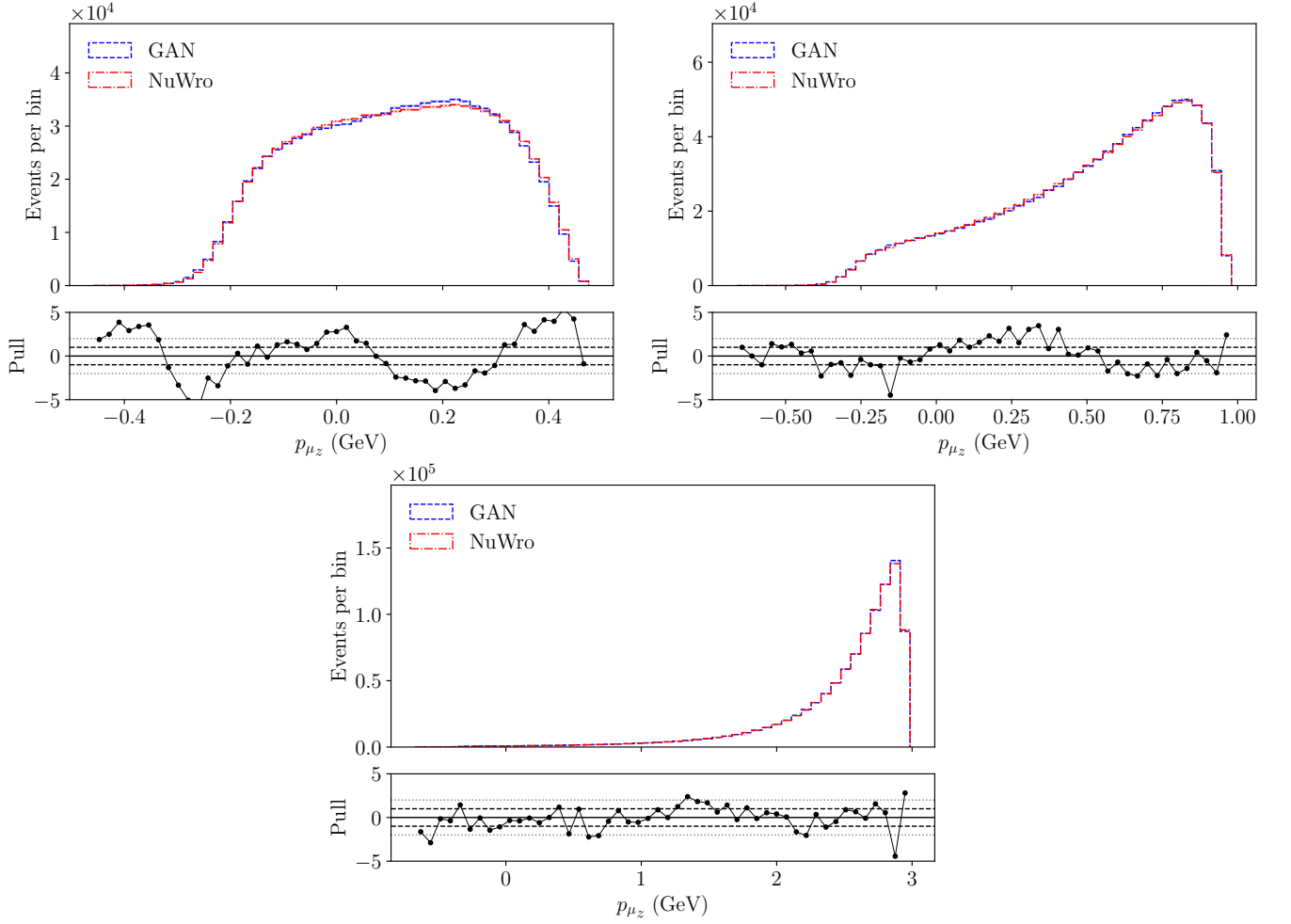


FIG. 12. Event histograms, depending on $p_{\mu,z}$ generated by the G-QE and NuWro for neutrino energies 0.5, 1, and 3 GeV, shown in top left, top right, and bottom figures, respectively.

TABLE I. EMD and MAP (with and without tails) computed for the samples generated by the NuWro and the G-QE for fixed neutrino energy E_ν and randomly sampled from a uniform E_ν distribution (“All” tag).

E_ν	EMD	MAP	MAP w/o tails
500 MeV	0.15	1.16	1.17
800 MeV	0.14	1.06	1.06
1 GeV	0.14	1.02	1.00
2 GeV	0.14	1.01	0.98
3 GeV	0.13	0.98	0.97
5 GeV	0.13	0.92	0.90
7 GeV	0.15	1.05	1.02
9 GeV	0.11	1.03	0.99
All	0.11	0.90	0.84

variables, both in the quasielastic (QE) region and at the peak of the $\Delta(1232)$ resonance. This consistency extends to the onset of deep inelastic (DIS) region in the histograms for $E_\nu = 5$ GeV.

TABLE II. Caption the same as in Table I but for INC model.

E_ν	EMD	MAP	MAP w/o tails
500 MeV	0.16	1.08	1.07
800 MeV	0.16	1.09	1.09
1 GeV	0.15	1.07	1.07
2 GeV	0.15	1.02	1.00
3 GeV	0.14	0.94	0.92
5 GeV	0.14	0.96	0.93
7 GeV	0.16	1.01	0.99
9 GeV	0.15	1.03	1.02
All	0.13	0.89	0.86

The numerical results for the INC model are summa-

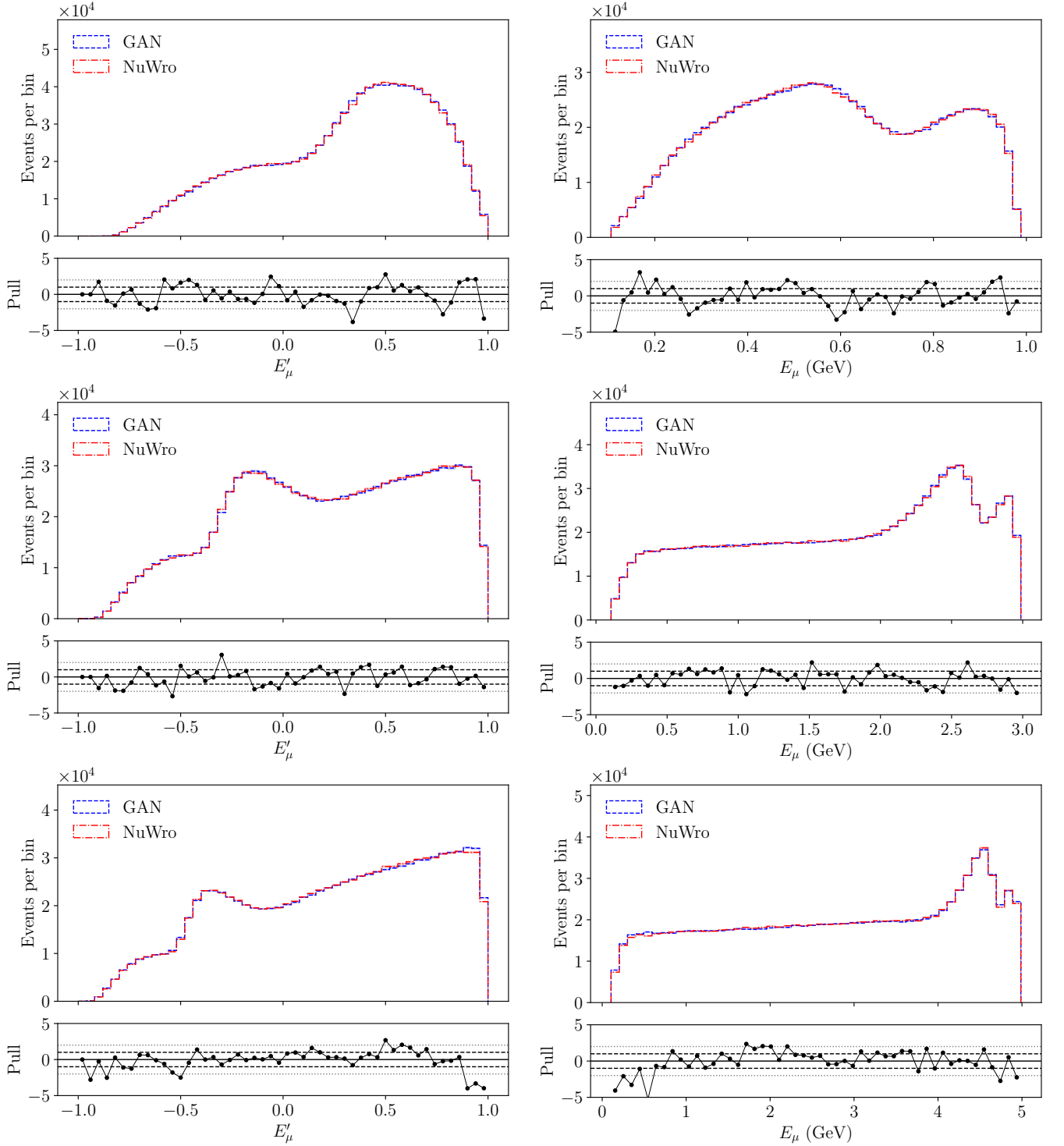


FIG. 13. Event histograms, depending on E'_μ (left column) and E_μ (right column) generated by the G-INC and the NuWro for neutrino energies = 1, 3, and 5 GeV, shown in top, middle and bottom rows, respectively.

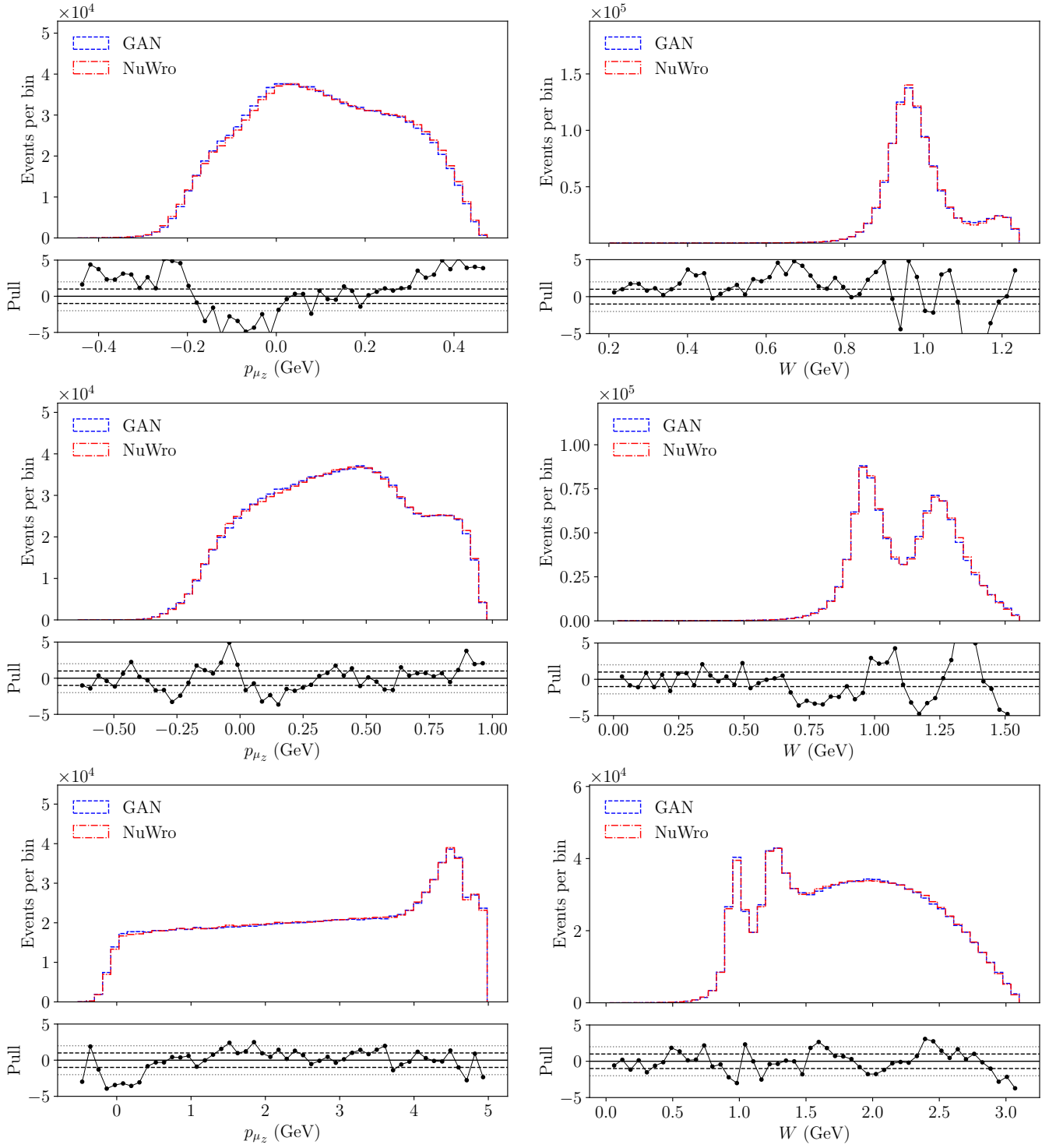


FIG. 14. Event histograms, depending on $p_{\mu,z}$ (left column) and hadronic invariant mass W (right column) generated by the G-INC and the NuWro for neutrino energies $E_\nu = 0.5, 1,$ and 5 GeV, shown in top, middle and bottom rows, respectively.

ized in Table II, where we present metrics EMD and MAP computed for test data sets generated for several values of the neutrino energies. The quality of performance of the G-INC model is as good as for the G-QE.

IV. SUMMARY

This article discusses the development of generative adversarial network models for simulating quasielastic and inclusive neutrino-nucleus scattering. The first type of

interaction plays a pivotal role in the oscillation analyses carried out by the T2K and Hyper-Kamiokande experiments, and the other is important for the DUNE experiment.

We consider various kinematic distributions of the charged lepton. The models we present successfully reproduce the peak structure in data distributions.

Once these models are developed, they generate events significantly faster than “classical” generators. We also anticipate that these models can be adapted to more realistic scenarios after retraining them on experimental data. Essentially, they can serve as pre-trained models that can be fine-tuned for specific applications.

Our study opens the door for future developments, including considering complete event topologies and realistic neutrino fluxes. Furthermore, these deep neural network models can be repurposed to simulate related

processes by utilizing advanced deep learning techniques such as transfer learning [15]. These studies are underway. Combining these ideas will hopefully lead to MC simulation tools that can improve their predictive precision by learning from new experimental measurements and theoretical considerations.

ACKNOWLEDGMENTS

This research is partly (K.M.G., A.M.A., J.T.S.) or fully (B.E.K., J.L.B., H.P., R.D.B.) supported by the National Science Centre under grant UMO-2021/41/B/ST2/ 02778.

K.M.G is partly supported by the “Excellence Initiative – Research University” for the years 2020-2026 at the University of Wrocław.

-
- [1] K. Abe *et al.* (T2K), *Nature* **580**, 339 (2020), [Erratum: *Nature* **583**, E16 (2020)], arXiv:1910.03887 [hep-ex].
- [2] R. Acciarri *et al.* (MicroBooNE), *JINST* **12** (02), P02017, arXiv:1612.05824 [physics.ins-det].
- [3] B. Abi *et al.* (DUNE), *Eur. Phys. J. C* **80**, 978 (2020), arXiv:2006.16043 [hep-ex].
- [4] K. Abe *et al.* (Hyper-Kamiokande Proto-Collaboration), *PTEP* **2015**, 053C02 (2015).
- [5] U. Mosel, *Annual Review of Nuclear and Particle Science* **66**, 171 (2016).
- [6] Y. Hayato and L. Pickering, *Eur. Phys. J. ST* **230**, 4469 (2021), arXiv:2106.15809 [hep-ph].
- [7] C. Andreopoulos *et al.*, *Nucl. Instrum. Meth. A* **614**, 87 (2010).
- [8] U. Mosel and K. Gallmeister, *Phys. Rev. C* **99**, 064605 (2019), arXiv:1811.10637 [nucl-ex].
- [9] C. Juszczak, J. A. Nowak, and J. T. Sobczyk, *Nucl. Phys. B Proc. Suppl.* **159**, 211 (2006), arXiv:hep-ph/0512365.
- [10] J. Isaacson, W. I. Jay, A. Lovato, P. A. N. Machado, and N. Rocco, *Phys. Rev. D* **107**, 033007 (2023), arXiv:2205.06378 [hep-ph].
- [11] J. M. Campbell *et al.*, *SciPost Phys.* **16**, 130 (2024), arXiv:2203.11110 [hep-ph].
- [12] L. Alvarez-Ruso, K. M. Graczyk, and E. Saul-Sala, *Phys. Rev. C* **99**, 025204 (2019), arXiv:1805.00905 [hep-ph].
- [13] O. Al Hammal, M. Martini, J. Frontera-Pons, T. H. Nguyen, and R. Pérez-Ramos, *Phys. Rev. C* **107**, 065501 (2023), arXiv:2305.08217 [nucl-th].
- [14] B. E. Kowal, K. M. Graczyk, A. M. Ankowski, R. D. Banerjee, H. Prasad, and J. T. Sobczyk, *Phys. Rev. C* **110**, 025501 (2024), arXiv:2312.17298 [hep-ph].
- [15] K. M. Graczyk, B. E. Kowal, A. M. Ankowski, R. D. Banerjee, J. L. Bonilla, H. Prasad, and J. T. Sobczyk, *Electron-nucleus cross sections from transfer learning* (2024), arXiv:2408.09936 [hep-ph].
- [16] J. E. Sobczyk, N. Rocco, and A. Lovato, *Phys. Lett. B* **859**, 139142 (2024), arXiv:2406.06292 [nucl-th].
- [17] M. El Baz and F. Sánchez, *Phys. Rev. D* **109**, 032008 (2024).
- [18] I. J. Goodfellow, J. Pouget-Abadie, M. Mirza, B. Xu, D. Warde-Farley, S. Ozair, A. Courville, and Y. Bengio, *Generative adversarial networks* (2014), arXiv:1406.2661 [stat.ML].
- [19] A. Nguyen, J. Clune, Y. Bengio, A. Dosovitskiy, and J. Yosinski, *Plug & play generative networks: Conditional iterative generation of images in latent space* (2017), arXiv:1612.00005 [cs.CV].
- [20] C. Ledig, L. Theis, F. Huszar, J. Caballero, A. Cunningham, A. Acosta, A. Aitken, A. Tejani, J. Totz, Z. Wang, and W. Shi, *Photo-realistic single image super-resolution using a generative adversarial network* (2017), arXiv:1609.04802 [cs.CV].
- [21] T. Salimans, I. Goodfellow, W. Zaremba, V. Cheung, A. Radford, X. Chen, and X. Chen, in *Advances in Neural Information Processing Systems*, Vol. 29, edited by D. Lee, M. Sugiyama, U. Luxburg, I. Guyon, and R. Garnett (Curran Associates, Inc., 2016).
- [22] I. Goodfellow, *Nips 2016 tutorial: Generative adversarial networks* (2017), arXiv:1701.00160 [cs.LG].
- [23] S. Badger *et al.*, *SciPost Phys.* **14**, 079 (2023), arXiv:2203.07460 [hep-ph].
- [24] L. de Oliveira, M. Paganini, and B. Nachman, *Comput. Softw. Big Sci.* **1**, 4 (2017), arXiv:1701.05927 [stat.ML].
- [25] J. W. Monk, *JHEP* **12**, 021, arXiv:1807.03685 [hep-ph].
- [26] A. Ghosh, X. Ju, B. Nachman, and A. Siodmok, *Phys. Rev. D* **106**, 096020 (2022), arXiv:2203.12660 [hep-ph].
- [27] P. Ilten, T. Menzo, A. Youssef, and J. Zupan, *SciPost Phys.* **14**, 027 (2023), arXiv:2203.04983 [hep-ph].
- [28] J. Chan, X. Ju, A. Kania, B. Nachman, V. Sangli, and A. Siodmok, *JHEP* **09**, 084, arXiv:2305.17169 [hep-ph].
- [29] Y. Alanazi *et al.*, *Phys. Rev. D* **106**, 096002 (2022), arXiv:2008.03151 [hep-ph].
- [30] J. T. Sobczyk, J. A. Nowak, and K. M. Graczyk, *Proceedings, 3rd International Workshop on Neutrino-nucleus interactions in the few GeV region (NUINT 04): Assergi, Italy, March 17-21, 2004*, *Nucl. Phys. Proc. Suppl.* **139**, 266 (2005), [,266(2004)], arXiv:hep-ph/0407277 [hep-ph].
- [31] T. Golan, J. T. Sobczyk, and J. Zmuda, *Nucl. Phys. B Proc. Suppl.* **229-232**, 499 (2012).
- [32] R. Das, L. Favaro, T. Heimel, C. Krause, T. Plehn, and D. Shih, *SciPost Phys.* **16**, 031 (2024), arXiv:2305.16774 [hep-ph].

- [33] Y. Rubner, C. Tomasi, and L. Guibas, in *Sixth International Conference on Computer Vision (IEEE Cat. No.98CH36271)* (1998) pp. 59–66.
- [34] O. Benhar, A. Fabrocini, S. Fantoni, and I. Sick, *Nucl. Phys. A* **579**, 493 (1994).
- [35] M. Mirza and S. Osindero, CoRR **abs/1411.1784** (2014), 1411.1784.
- [36] F. Chollet *et al.*, Keras, <https://keras.io> (2015).
- [37] J. L. Ba, J. R. Kiros, and G. E. Hinton, Layer normalization (2016), arXiv:1607.06450 [stat.ML].
- [38] H. Li, Z. Xu, G. Taylor, C. Studer, and T. Goldstein, in *Advances in Neural Information Processing Systems*, Vol. 31, edited by S. Bengio, H. Wallach, H. Larochelle, K. Grauman, N. Cesa-Bianchi, and R. Garnett (Curran Associates, Inc., 2018).
- [39] A. L. Maas, in *Proceedings of the 30th International Conference on Machine Learning, Vol. 28, 3.* (2013).
- [40] X. Glorot, A. Bordes, and Y. Bengio, in *Proceedings of the Fourteenth International Conference on Artificial Intelligence and Statistics*, Proceedings of Machine Learning Research, Vol. 15, edited by G. Gordon, D. Dunson, and M. Dudík (PMLR, Fort Lauderdale, FL, USA, 2011) pp. 315–323.
- [41] K. He, X. Zhang, S. Ren, and J. Sun, arXiv e-prints , arXiv:1502.01852 (2015), arXiv:1502.01852 [cs.CV].
- [42] R. Feng, D. Zhao, and Z.-J. Zha, in *Proceedings of the 38th International Conference on Machine Learning*, Proceedings of Machine Learning Research, Vol. 139, edited by M. Meila and T. Zhang (PMLR, 2021) pp. 3284–3293.
- [43] I. Goodfellow, Y. Bengio, and A. Courville, *Deep Learning* (MIT Press, 2016) <http://www.deeplearningbook.org>.
- [44] L. Demortier and L. Lyons, e-Print (2008).